
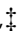






Cite this: DOI: 10.1039/d2nr05666f

Two -dimensional semimetal AlSb monolayer with multiple nodal-loops and extraordinary transport properties under uniaxial strain†

Qian Xia,  ‡ Na Li,  ‡ Wei-Xiao Ji,  * Chang-Wen Zhang, Meng Ding, Miao-Juan Ren and Sheng-Shi Li  *

Two-dimensional (2D) nodal-loop semimetal (NLSM) materials have attracted much attention for their high-speed and low-consumption transporting properties as well as their fantastic symmetry protection mechanisms. In this paper, using systematic first-principles calculations, we present an excellent NLSM candidate, a 2D AlSb monolayer, in which the conduction and valence bands cross with each other forming fascinating multiple nodal-loop (NL) states. The NLSM properties of the AlSb monolayer are protected by its glide mirror symmetry, which was confirmed using a symmetry-constrained six-band tight-binding model. The transport properties of the AlSb monolayer under in-plane uniaxial strains are also studied, based on a non-equilibrium Green's function method. It is found that both compressive and tensile strains from -10% to 10% improve the transporting properties of AlSb, and it is interesting to see that flexure configurations are energetically favored when compressive uniaxial strains are applied. Our studies not only provide a novel 2D NLSM candidate with a new symmetry protection mechanism, but also raise the novel possibility for the detection of out-of-plane flexure in 2D semimetal materials.

Received 12th October 2022,
Accepted 13th December 2022

DOI: 10.1039/d2nr05666f

rsc.li/nanoscale

1. Introduction

Nodal-loop semimetals (NLSM)^{1–3} have attracted plenty of attention in the recent years, for both their research significance in fundamental physics and their potential applications in next-generation nanoscale spintronic devices. The gapless band crossings in NLSM, unlike the discrete crossing points in Dirac/Weyl semimetals,^{4–7} form continuous open or closed loops in the momentum space, which is protected by certain crystal symmetries. These unique band characteristics are expected to be associated with intriguing physics, such as drumhead surface states, high-temperature surface superconductivity⁸ and anomalous quantum oscillation.⁹ Three-dimensional (3D) NLSM material candidates, such as Ti₃Al, Cu₃PdN and TiB₂, have been demonstrated theoretically and experimentally.^{10–18} However, the search for two-dimensional (2D) NLSMs is still challenging due to these materials having reduced crystal symmetry in comparison to the 3D examples. Several 2D monolayers, such as Si-Cmma, B₂O, TaSiTe₆ and MnB,^{19–26} were predicted theoretically to be NLSM, and some,

such as Cu₂Si, CuSe and GaAg,^{27–29} have been synthesized successfully in experiments and verified as NLSM materials using angle-resolved photoemission spectroscopy. It is worth mentioning that most of the aforementioned 2D NLSM candidates have gapless nodal-loops (NLs) protected by their horizontal mirror symmetries. This symmetry protection mechanism has been expanded to nonsymmorphic glide mirror symmetry recently, for example, in MnNF and NiB₂ monolayers.^{30,31} To date, the number of known 2D NLSM materials is still limited. Moreover, the excellent conductivity of NLSM materials indicates their potential for application in high-speed and low dissipation nanoscale electronic and spintronic devices, although research on their transport properties and devices based on 2D NLSM materials is scarce at present. We have also noticed the recent theoretical⁵⁰ and experimental⁴⁸ progress on the wrinkling characteristics of 2D materials under compressive strains, which provides a new approach for us to modulate the transport properties of 2D NLSM materials. Consequently, it is urgent and of significance to find novel 2D NLSM materials, propose new mechanisms of symmetry protection in 2D nodal-loops, and design high-efficiency and multipurpose spintronic devices.

In this paper, we propose an AlSb monolayer as a novel 2D NLSM candidate material, based on first-principles (FP) calculations and a tight-binding (TB) model. The band structure reveals that the band crossing forms multiple nodal-loops

Spintronics Institute & School of Physics and Technology, University of Jinan, Jinan, Shandong 250022, P. R. China. E-mail: sps_jiwx@ujn.edu.cn, sdy_liss@ujn.edu.cn

† Electronic supplementary information (ESI) available. See DOI: <https://doi.org/10.1039/d2nr05666f>

‡ These authors contributed equally to this work.

around the Γ point near the Fermi level, whilst, according to the symmetry analysis on wavefunctions and a symmetry-restricted six-band TB model that we developed, the nodal-loops are demonstrated to be protected by nonsymmorphic horizontal glide mirror symmetry. Meanwhile, we design a nanoscale device based on the AlSb monolayer and investigate its transport properties under uniaxial strains. It is found that the conductivity of the device generally increases under both compressive and tensile strains, and it is also interesting to see that the formation of the out-of-plane flexure is energetically favored when compressive strains are applied. Our studies provide not only a novel 2D NLSM candidate material, but also significant support for the potential applications of NLSM materials in transporting devices and flexing mechanical sensors.

2. Computational details

Density-functional theory (DFT) calculations were carried out based on a projector augmented wave (PAW) approach,³² as implemented in the Vienna *Ab initio* Simulation Package (VASP)^{33,34} and DS-PAW package.³⁵ For the exchange–correlation functional, a generalized gradient approximation (GGA) with Perdew–Burke–Ernzerhof (PBE) realization was adopted.^{36,37} In addition, a more reliable Heyd–Scuseria–Ernzerhof (HSE06) hybrid functional³⁸ was employed for the validation of band structures. The energy cutoff was set to be 550 eV and a vacuum layer of 20 Å was added to avoid interaction along the out-of-plane direction. The equilibrium positions of the atoms as well as the lattice constants were fully optimized until the energy and the force converged to less than 10^{-8} eV and 0.0001 eV Å⁻¹, respectively. The Brillouin zone (BZ) was sampled using a $19 \times 19 \times 1$ Γ -centered Monkhorst–Pack k -point mesh. The phonon dispersion spectrum was calculated based on a supercell approach performed with ALAMODE code.³⁹ An unbiased swarm-intelligence structural method based on the particle swarm optimization (PSO) technique implemented in the CALYPSO package^{40–44} was employed to search for low-energy structures of AlSb. The transport properties were investigated using DFT combined with the nonequilibrium Green's Function (NEGF) method, as implemented in the Nanocal package,^{45,46} in which the cutoff energy is set to 100 Rydberg (1361 eV), the temperature of electrode is set to 100 K and the k -point grid mesh of the electrode is set to $100 \times 8 \times 1$. The current was calculated using the Landauer–Büttiker equation:⁴⁷

$$I(V_b) = \frac{2e}{h} \int_{\mu_L}^{\mu_R} T(E, V_b) [f_L(E) - f_R(E)] dE$$

in which $f_{L(R)}$ is the distribution function of electrons on left (right) lead, V_b is the bias voltage, and $\mu_{L(R)}$ is the potential of left (right) lead. $T(E, V_b)$ is the transmission coefficient given by $T(E, V_b) = T[\Gamma_L G^r \Gamma_R G^a]$, where $G^{r(a)}$ is the retarded (advanced) Green's function of the scattering region and $\Gamma_{L(R)} = i[\Sigma_{L(R)}^r - \Sigma_{L(R)}^a]$ is the self-energy of the left (right) lead.

3. Results and discussion

3.1. Geometric structure and stability

The top and side views of the optimized geometrical structure of the AlSb monolayer are presented in Fig. 1(a). It has a rectangular lattice belonging to the space group $P4/nmm$ (D_{4h}^7 , No. 129), with each unit cell containing two Al and two Sb atoms. The lattice constants are optimized to be $a = b = 4.22$ Å. It is noteworthy that the AlSb monolayer prefers a buckled structure, without horizontal mirror symmetry. All the Al atoms are located in the central plane and two Sb atoms are alternately located at the upper and lower surfaces, with the buckle height being 3.59 Å. Each Al (Sb) atom is coordinated by four Sb (Al) atoms, forming a four-coordinate structure.

The structural stability of the AlSb monolayer was checked symmetrically. Firstly, the elastic moduli were calculated to be $C_{11} = 190.09$ N m⁻¹, $C_{12} = 96.06$ N m⁻¹, $C_{22} = 190.09$ N m⁻¹, and $C_{44} = 33.02$ N m⁻¹, which satisfy Born's criteria ($C_{11} > 0$, $C_{11}C_{22} > C_{12}^2$, and $C_{44} > 0$). Secondly, the phonon spectra of the AlSb monolayer were calculated and are depicted in Fig. 1(b). There is no imaginary mode of lattice vibration in the first BZ, which validates the dynamical stability of AlSb monolayer. Next, *ab initio* molecular dynamics (AIMD) simulations were performed at 300 K using a 4×4 supercell in order to check the stability of AlSb at ambient conditions. The results show that the total energy of the AlSb monolayer fluctuates smoothly over specific energy intervals after 10 ps of preheating (see Fig. 1(c)). Equally, no structural reconstruction and lattice collapse are observed, as illustrated by the snapshots in Fig. S1 of the ESI,[†] which indicates the thermal stability of the AlSb

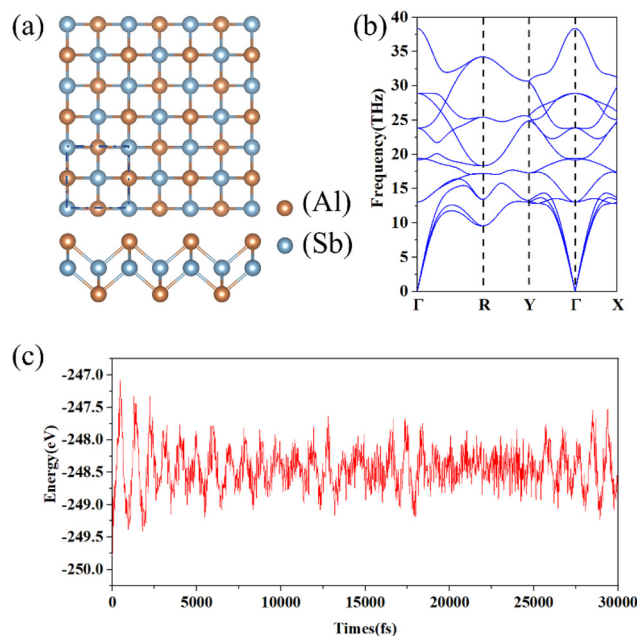


Fig. 1 (a) Top and side views of the optimized structure of the AlSb monolayer. (b) Calculated phonon dispersion of the AlSb monolayer. (c) Variation in total energy for AlSb monolayer at 300 K during an AIMD simulation.

monolayer at room temperature. Furthermore, we performed a global structural optimization by means of a PSO method (the five configurations with lowest energy are listed in Table S1 of the ESI†) and it was found that the configuration of ALSb we predicted above has the second lowest energy, which is only 0.028 eV per atom higher than the global minimum. All the results above demonstrate the stability of the ALSb monolayer and imply the possibility that it can be experimentally synthesized.

Then we studied the mechanical characteristic of the ALSb monolayer. The in-plane Young's modulus and Poisson's ratio along an arbitrary direction ϕ are calculated using the following formulae:

$$Y(\phi) = \frac{C_{11}C_{22} - C_{12}^2}{C_{11}s^4 + C_{22}c^4 + \left(\frac{C_{11}C_{22} - C_{12}^2}{C_{44}} - 2C_{12}\right)c^2s^2}$$

$$\nu(\phi) = -\frac{\left(C_{11} + C_{22} - \frac{C_{11}C_{22} - C_{12}^2}{C_{44}}\right)c^2s^2 - C_{12}(c^4 + s^4)}{C_{11}s^4 + C_{22}c^4 + \left(\frac{C_{11}C_{22} - C_{12}^2}{C_{44}} - 2C_{12}\right)c^2s^2}$$

where $c = \cos \phi$ and $s = \sin \phi$. The corresponding results are plotted in Fig. 2. Note that the minimum value of the Young's modulus (108 N m^{-1}) is still larger than that of silicene (62 N m^{-1}),¹ which would lead to considerable in-plane stiffness and strong bonding between atoms.

3.2. Electronic structures and nodal-loops

The electronic properties of the ALSb monolayer were investigated *via* spin-polarized self-consistent calculations with fully optimized configurations. Following these calculations the ALSb monolayer was found to be nonmagnetic. The electronic band structure is shown in Fig. 3(a). It can be seen that the conduction and valence bands meet in the vicinity of the Fermi level and form three linear band crossings, located at $P_1(0.05, 0.05, 0.00)$ along Γ -R, $P_2(0.00, 0.10, 0.00)$ along Y- Γ , and $P_3(0.10, 0.00, 0.00)$ along Γ -X, respectively. Typical type-II Dirac nodal points are observed, which can be further verified using a more reliable HSE06 functional, as shown in Fig. S2 of the ESI.† By projecting the energy bands near the Fermi level into different atomic orbitals, it can be seen that the Al s orbital and Sb p orbital predominantly contribute to the electronic

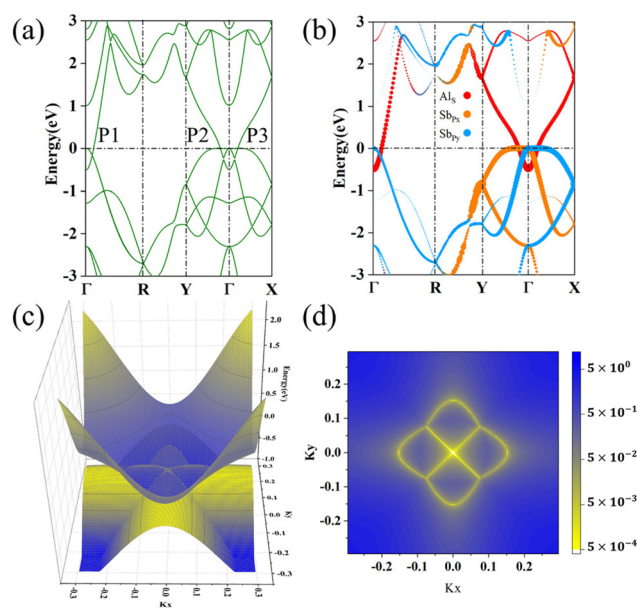


Fig. 3 (a) Energy band structure of ALSb. (b) Corresponding orbital-resolved projection. (c) The three crossing bands forming the multiple NLs. (d) The gaps between bands, illustrating the distribution of NLs in the whole BZ.

states, as shown in Fig. 3(b). The band crossing around the Γ point suggests the existence of NL properties, which is visualized by the band structure plot in the whole BZ, as shown in Fig. 3(c) and (d). It can be found that the intersection of the conduction band minimum (CBM) and the valence band maximum (VBM) forms multiple closed NLs shaped like a window, illustrating anisotropy in the momentum space. Furthermore, the linear band dispersion endows the NL state with a considerable Fermi velocity of $2.09 \times 10^5 \text{ m s}^{-1}$ in the a direction and massless fermions at the Fermi level, indicating good electroconductivity. In addition, we also studied the Seebeck coefficient of ALSb monolayer to check the potential thermoelectric properties that are observed in many topological materials.^{51,52} The results are plotted in Fig. S8 of the ESI.† Unfortunately, the Seebeck coefficient of ALSb ($\sim 60 \mu\text{V K}^{-1}$) is orders of magnitude lower than that of other typical 2D thermoelectric materials, such as black phosphorus ($\sim 2000 \mu\text{V K}^{-1}$) and GeS ($\sim 2800 \mu\text{V K}^{-1}$), indicating that the ALSb monolayer is unlikely to have good thermoelectric performance.

The mechanism for perfect conducting properties was explored *via* the charge differential density (CDD) and electronic localization function (ELF), as shown in Fig. 4. Electrons transfer from the Al atoms to the Sb atoms, with the amount of charge transfer estimated to be $1.35e$ from a Bader population analysis, indicating the formation of strong polarized covalent bonds. The electrons located in the Al plane are analogous to a free electronic gas according to the ELF results, and there are highly localized lone pair electrons pointing outward from the monolayer around the Sb atoms. In combination with the band structure, it could be confirmed that the

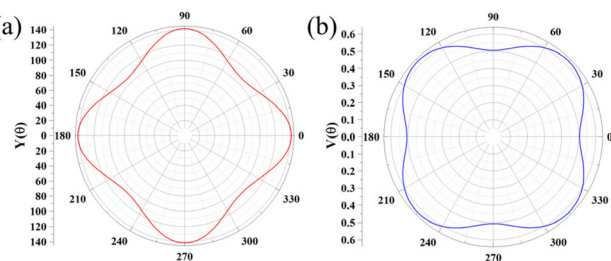


Fig. 2 (a) Young's modulus and (b) Poisson's ratio of the ALSb monolayer.

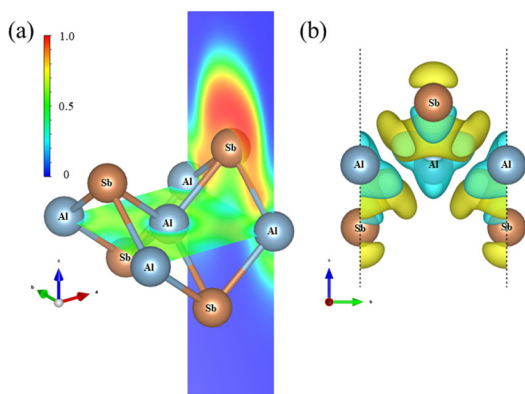


Fig. 4 (a) The ELF and (b) the CDD of the AlSb monolayer (with an iso-surface of $0.004 \text{ e} \text{ \AA}^{-3}$).

conducting properties are mainly determined by the nearly free electrons around the Al skeleton.

3.3. NL symmetry protection mechanism

Next, we focused on elucidating the NL state symmetry protection mechanism. In the case of two-dimensional materials, the nodal-loop is protected by a horizontal mirror reflecting operator M_z , which ensures a gapless band crossing at any arbitrary k -points in the loop. The configuration of the AlSb monolayer belongs to the $P4/nmm$ space group, which contains sixteen symmetry operators, including five rotational axes $\{C_{2z}, C_{4z}, C_{2d}\}$, three vertical mirror planes $\{M_x, M_y, M_d\}$, two screw axes $\left\{C_{2x} \left| \frac{1}{2} 0 \right.\right\}$ and $\left\{C_{2y} \left| 0 \frac{1}{2} \right.\right\}$, one inversion center (I) and one glide mirror $g_z = \left\{M_z \left| \frac{1}{2} \frac{1}{2} \right.\right\}$, as well as time-reversal (TR) symmetry. Clearly, it is only the glide mirror symmetry g_z that contains the horizontal mirror operator M_z , and therefore it plays an indispensable role in the protection of the nodal-loop in the AlSb monolayer. To illustrate this protection mechanism clearly, the real-space Kohn–Sham wavefunction near the band crossing points is shown in Fig. S3,[†] from which the eigenvalue of g_z for each band could be obtained and labelled as + and – (representing $\pm i$) respectively. Consequently, the two intersecting bands have opposite glide mirror eigenvalues, indicating that they are mutually orthogonal without any hybridization and that the formation of a gapless NL is inevitable.

From the FP investigations, we know that the dominant components of the NL are the Al-s and Sb- p_x, p_y orbitals, whereas the contributions from the Sb-s/ p_z and Al-p orbitals are negligible, as shown in Fig. 3(b) and S5.[†] Taking $s^{\text{Al1}}, s^{\text{Al2}}, p_x^{\text{Sb1}}, p_x^{\text{Sb2}}, p_y^{\text{Sb1}}, p_y^{\text{Sb2}}$ as the basis

$$H(k) = \begin{bmatrix} h_1 & h_{11} & 0 & 0 & 0 & 0 \\ h_{11}^\dagger & h_1 & 0 & 0 & 0 & 0 \\ 0 & 0 & h_2 & 0 & 0 & 0 \\ 0 & 0 & 0 & h_3 & 0 & 0 \\ 0 & 0 & 0 & 0 & h_2 & 0 \\ 0 & 0 & 0 & 0 & 0 & h_3 \end{bmatrix},$$

in which

$$h_1 = 2t_{s2}(\cos(ak_x) + \cos(ak_y)) + \varepsilon_s,$$

$$h_{11} = h_{11}^\dagger = 2t_{s1} \left(\cos\left(\frac{ak_x}{2}\right) + \cos\left(\frac{ak_y}{2}\right) \right),$$

$$h_2 = 2t_\pi \cos(ak_y) + 2t_\sigma \cos(ak_x) + \varepsilon_p,$$

$$h_3 = 2t_\pi \cos(ak_x) + 2t_\sigma \cos(ak_y) + \varepsilon_p,$$

and $\varepsilon_s, \varepsilon_p$ are the on-site energies corresponding to the s orbital of Al and the p orbitals of Sb, t_{s1} and t_{s2} are the parameters for the hopping of the s orbitals between the nearest- and second-nearest-neighboring Al–Al, and t_σ and t_π are the parameters for the hopping between the p orbitals of the nearest-neighboring Sb–Sb. The family of the Hamiltonian can be written as

$$H(k) = \varepsilon_s \times U_1 + \varepsilon_p \times U_2 + t_1 \times U_3 + t_2 \times U_4 + t_s \times U_5 + t_p \times U_6$$

and the detailed matrices can be found in the ESI.[†] The strict orthogonality of the Al-s and Sb-p orbitals is clear to see in $H(k)$, demonstrating that the formation of the NL states is not occasional but protected by the structural symmetry. The valence and conduction bands are fitted according to the first-principles results in the entire BZ *via* an unbiased least-squares method, with all the parameters listed in Table S2 of the ESI.[†] The results near the Γ point agree well with those from the FP results, as shown in Fig. 5(a).

The spin-orbit coupling (SOC) effects were introduced by considering only the on-site contribution, *i.e.*, the $L \times S$ term from the Sb-p orbitals. Thus, we get the SOC contribution to the Hamiltonian, using the bases $|l\uparrow\rangle, |l\downarrow\rangle$, as

$$H' = \lambda L \times S,$$

where λ characterizes the strength of the SOC. The TB Hamiltonian with SOC is as follows:

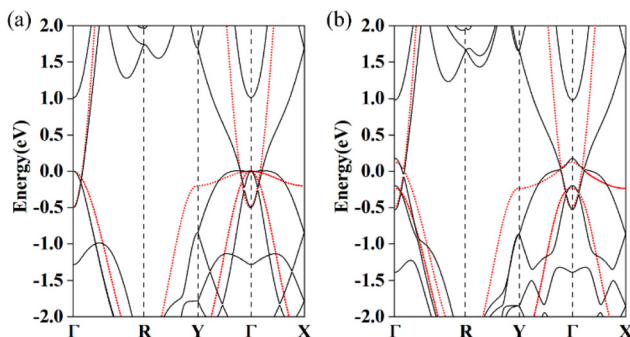


Fig. 5 Electronic band structures from first-principles (black line) and a tight-binding model (red dotted line) (a) without and (b) with SOC.

$$H_{\text{soc}}(k) = \begin{bmatrix} 0 & 0 & 0 & 0 & 0 & 0 \\ 0 & 0 & 0 & 0 & 0 & 0 \\ 0 & 0 & 0 & h & 0 & 0 \\ 0 & 0 & h^\dagger & 0 & 0 & 0 \\ 0 & 0 & 0 & 0 & 0 & h \\ 0 & 0 & 0 & 0 & h^\dagger & 0 \end{bmatrix} + H(k),$$

in which

$$h = \begin{bmatrix} -\frac{i}{2}\lambda & 0 \\ 0 & \frac{i}{2}\lambda \end{bmatrix}$$

with $\lambda = 0.09$ eV. We find that the SOC splits the band degeneracy around point Γ near the Fermi level. The bands from the TB Hamiltonians with SOC are shown in Fig. 5(b) and agree well with the FP results in the entire BZ.

3.4. Band engineering by symmetry breaking and protection

The symmetry protection mechanism could be employed for band engineering of the nodal-loops, for example, the transition between a nodal-loop and other states. As shown in Fig. S4 of the ESI† we tested two distorted configurations in which the glide mirror and vertical mirror symmetry were broken and observed the band gap opening of the NL in both cases. Then, a vertical electric field was applied, which is a more reliable way in experiments to realize the modulation of the NL state. Under the effects of the electric field, the symmetries of the glide mirror g_z and in-plane rotation C_{2d} are consequently broken. The new family of Hamiltonians has two additional terms (U_7 and U_8 , see the ESI† for details), leading to coupling between the Al and Sb orbitals and then the breaking of the nodal-lines. These results were further confirmed using DFT calculations in which an electric field of 0.5 V \AA^{-1} is applied along the c direction. As plotted in Fig. S6,† the nodal-loop degenerates to discrete nodal points, indicating the occurrence of a tunable topological transition. Considering a typical environment for experimental synthesis and application, we introduced two oxygens per unit cell on top of the Sb atoms to passivate the dangling bonds⁴⁹ without breaking the glide

mirror symmetry. The optimized structure is shown in Fig. 6(a) in which the nodal-loop state is well preserved, as shown in Fig. 6(b). Furthermore, we applied in-plane biaxial strains to investigate whether the energy level of the nodal-loop state could be modulated. Here, the strain is defined as $\varepsilon_a = (a - a_0)/a_0$, in which a_0/a represents the lattice constant without/with strain engineering. The energy band structure of AlSb is well preserved in strains from -3% to 3% . Fig. S7 of the ESI† shows the energy band structure under different strains, where it is found that the nodal loop, under a compressive strain of 2% , can be moved to the Fermi level without being covered by other bands, as shown in Fig. 6(c).

3.5. Transport properties under uniaxial strains

Considering the potential excellent conductive characteristics of NLSMs, the transport properties of an AlSb nanodevice was studied. The design of the device is shown in Fig. 7(a). Due to the isotropy of the structure, we focused on the uniaxial strains along the a direction (x -axis), and expanded the unit cell by 20 times along the a direction, with the length of the device a_0 being 8.44 nm. The current–voltage (I – V) curve of the device under different bias voltages (over the range of 0.2 to 2.0 V) were calculated and plotted in Fig. 7(c) with black dots. It was found that the I – V curve could be divided into two parts. It has an approximate horizontal platform from 0.2 to 1.0 V which can be understood by the transmission coefficient analysis. Although the energy windows broaden dramatically from 0.2 to 1.0 V, as shown in Fig. 7(d), the integral transmission does not obviously increase, resulting in a nearly unchanged current as the bias voltage increases. By contrast, the current presents a nearly linear increase as a function of bias voltage over the range from 1.2 to 2.0 V, illustrating an ideal Ohm relationship.

As strain is a commonly used method to modulate the electronic properties of 2D materials, we studied the behaviors of AlSb under tensile and compressive uniaxial strains along the a direction, as illustrated in Fig. 7(a). The strain value ε is defined as $\varepsilon = (a - a_0)/a_0$, where a is the lattice constant along

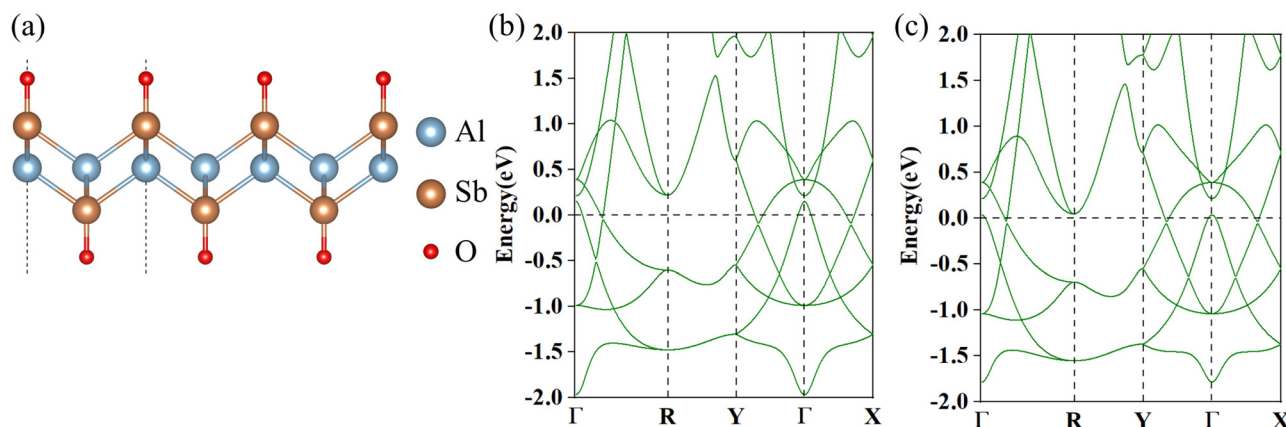


Fig. 6 (a) The structure of oxidized AlSb, with the dangling bonds on the Sb atoms saturated by oxygen. (b) The energy band structure of the oxidized AlSb monolayer. (c) The band structure obtained for an oxidized AlSb monolayer under a compressive strain of 2% .

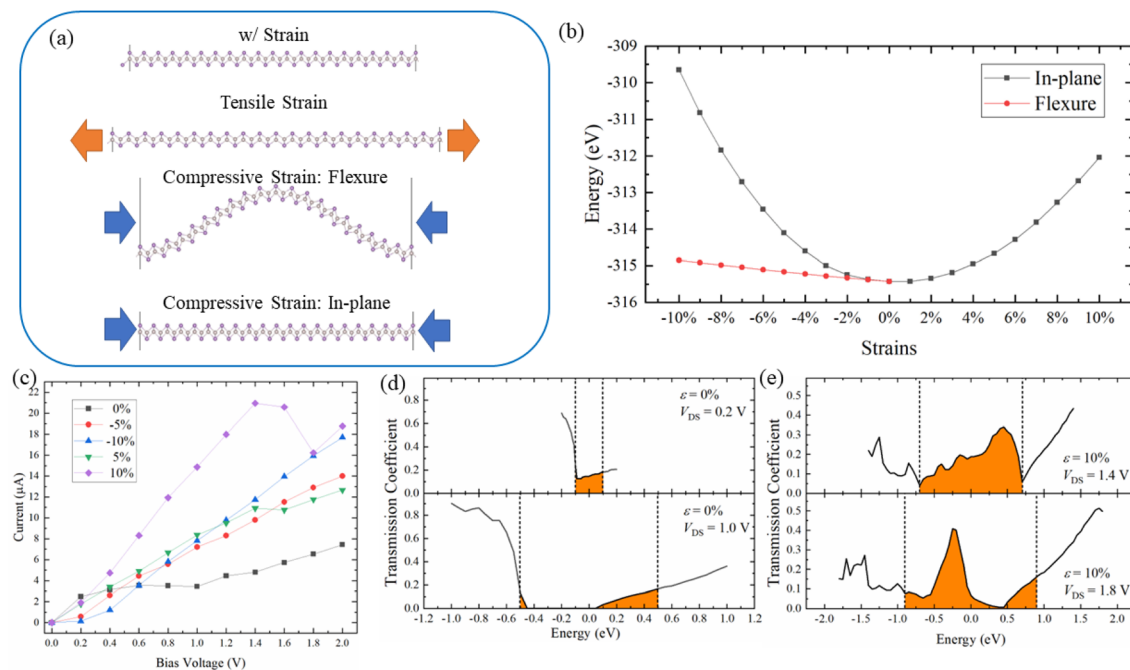


Fig. 7 (a) The design of the AlSb device. (b) The energy as a function of strain between two configurations. (c) The current–voltage curve of the AlSb device under tensile and compressive strains. (d and e) The transmission coefficient as a function of the energy under different strains.

the x -axis with strain, and a_0 is 8.44 nm without strain. The tensile strains are easy to apply, however an out-of-plane deformation might occur when compressive strains are applied, and therefore the energy of different configurations should be compared. Fig. 7(b) shows the energy as a function of strain. In the compressive strain cases (*i.e.*, $\varepsilon < 0$) the configurations with out-of-plane flexures have an obviously lower energy than the in-plane cases, illustrating a linear energy-strain relationship, which indicates that the configurations with flexures occur much more easily than when compressive strains are applied.

The I - V curve of the AlSb device under tensile and compressive strains is also plotted in Fig. 7(c). In general, the currents of the device under both compressive and tensile strains are larger than that without strains, except for the lower bias voltage (0.2 V), indicating that the improved transport properties caused by strain. The behaviors of the current under tensile strains of 5% (green dots) and 10% (purple dots) look similar. The current increases with the increase in tensile strain, while the I - V relation below 1.4 V is almost linear, and a negative differential resistance (NDR) occurs in both cases at 1.6 V. The NDR effect is more obvious under a tensile strain of 10%, and it can be understood by analyzing the transmission spectra. As shown in Fig. 7(e), the voltage window grows wider as the bias voltage increases, while the transmission decreases and it leads to the NDR effect. When compressive strains of 5% (red dots) and 10% (blue dots) are applied, the out-of-plane flexure forms, as mentioned above. In such cases, the I - V curves are similar, that is a parabolic relationship below 0.4 V, and a nearly linear I - V curve from 0.4 to 2.0 V. The current under a 5% compressive strain is higher than that under a

10% compressive strain when the bias voltage is lower than 0.8 V, but this situation is reversed when the bias voltage is higher than 0.8 V. This strain-electric coupling mechanism could be applied in flexing mechanical sensors.

4. Conclusions

In summary, using first-principles calculations combined with a tight-binding (TB) method, we propose a novel 2D nodal-loop semimetal namely an AlSb monolayer. The favorable dynamic and thermal stabilities, as well as the results from a global minimum search, suggest with high probability that the AlSb monolayer can be fabricated experimentally. Also, we have developed a symmetry-restricted six-band TB model that could sufficiently capture the band properties of the AlSb monolayer in the Brillouin zone, and verified that the nodal-loop is protected by the horizontal glide mirror symmetry of the material. We also confirmed that the nodal-loop could be further modulated by breaking the symmetry, for example, in a vertical electric field. In order to discover possible applications of AlSb in nanoscale conductive devices, we studied the transporting properties of the AlSb monolayer under uniaxial compressive and tensile strains. We found several interesting conductive phenomena, such as a conductive platform without strain, the improvement of conductivity under both compressive and tensile strains, and a negative differential resistance effect under tensile strains. It is also interesting to see that AlSb prefers a configuration with flexure when compressive strains are applied, which could be applied in the detection of

out-of-plane flexures. Our results provide a desirable platform for exploring the fascinating physics and novel protection mechanisms of nodal-loop states, which simultaneously broadens the scope of 2D transporting devices.

Conflicts of interest

The authors declare that they have no conflict of interest.

Acknowledgements

This work is supported by the National Natural Science Foundation of China (Grant No. 12004137, 12104183, 62071200), Shandong Provincial Natural Science Foundation (Grant No. ZR2022MB142, ZR2020QA052, ZR2021MA040, ZR2019MA041, ZR2021MA060), Taishan Scholar Program of Shandong Province (Grant No. ts20190939), and Independent Cultivation Program of Innovation Team of Jinan City (Grant No. 2021GXRC043). We thank Xiaowen Shi and Mingyan Chen from HZWTECH for help and discussions regarding this study.

References

- 1 Y. Ding and Y. Wang, *J. Phys. Chem. C*, 2013, **117**, 18266.
- 2 Y. Kim, B. J. Wieder, C. Kane and A. M. Rappe, *Phys. Rev. Lett.*, 2015, **115**, 036806.
- 3 K. Mullen, B. Uchoa and D. T. Glatzhofer, *Phys. Rev. Lett.*, 2015, **115**, 026403.
- 4 A. Burkov, M. Hook and L. Balents, *Phys. Rev. B: Condens. Matter Mater. Phys.*, 2011, **84**, 235126.
- 5 S. Borisenko, Q. Gibson, D. Evtushinsky, V. Zabolotnyy, B. Büchner and R. J. Cava, *Phys. Rev. Lett.*, 2014, **113**, 027603.
- 6 Z. K. Liu, J. Jiang, B. Zhou, Z. J. Wang, Y. Zhang, H. M. Weng, D. Prabhakaran, S. K. Mo, H. Peng, P. Dudin, T. Kim, M. Hoesch, Z. Fang, X. Dai, Z. X. Shen, D. L. Feng, Z. Hussain and Y. L. Chen, *Nat. Mater.*, 2014, **13**, 677.
- 7 Z. K. Liu, B. Zhou, Y. Zhang, Z. J. Wang, H. M. Weng, D. Prabhakaran, S. K. Mo, Z. X. Shen, Z. Fang, X. Dai, Z. Hussain and Y. L. Chen, *Science*, 2014, **343**, 864.
- 8 B. Q. Lv, N. Xu, H. M. Weng, J. Z. Ma, P. Richard, X. C. Huang, L. X. Zhao, G. F. Chen, C. E. Matt, F. Bisti, V. N. Strocov, J. Mesot, Z. Fang, X. Dai, T. Qian, M. Shi and H. Ding, *Nat. Phys.*, 2015, **11**, 724.
- 9 N. Kopnin, T. Heikkilä and G. Volovik, *Phys. Rev. B: Condens. Matter Mater. Phys.*, 2011, **83**, 220503.
- 10 C. Li, C. Wang, B. Wan, X. Wan, H.-Z. Lu and X. Xie, *Phys. Rev. Lett.*, 2018, **120**, 146602.
- 11 X. Zhang, Z.-M. Yu, Z. Zhu, W. Wu, S.-S. Wang, X.-L. Sheng and S. A. Yang, *Phys. Rev. B*, 2018, **97**, 235150.
- 12 R. Yu, H. Weng, Z. Fang, X. Dai and X. Hu, *Phys. Rev. Lett.*, 2015, **115**, 036807.
- 13 H. Weng, Y. Liang, Q. Xu, R. Yu, Z. Fang, X. Dai and Y. Kawazoe, *Phys. Rev. B: Condens. Matter Mater. Phys.*, 2015, **92**, 045108.
- 14 Z. Liu, R. Lou, P. Guo, Q. Wang, S. Sun, C. Li, S. Thirupathiah, A. Fedorov, D. Shen, K. Liu, H. Lei and S. Wang, *Phys. Rev. X*, 2018, **8**, 031044.
- 15 H. Huang, K.-H. Jin and F. Liu, *Phys. Rev. B*, 2017, **96**, 115106.
- 16 L. M. Schoop, M. N. Ali, C. Straßer, A. Topp, A. Varykhalov, D. Marchenko, V. Duppel, S. S. P. Parkin, B. V. Lotsch and C. R. Ast, *Nat. Commun.*, 2016, **7**, 11696.
- 17 Y. Wu, L.-L. Wang, E. Mun, D. D. Johnson, D. Mou, L. Huang, Y. Lee, S. L. Bud'ko, P. C. Canfield and A. Kaminski, *Nat. Phys.*, 2016, **12**, 667.
- 18 G. Bian, T.-R. Chang, R. Sankar, S.-Y. Xu, H. Zheng, T. Neupert, C.-K. Chiu, S.-M. Huang, G. Chang, I. Belopolski, D. S. Sanchez, M. Neupane, N. Alidoust, C. Liu, B. Wang, C.-C. Lee, H.-T. Jeng, C. Zhang, Z. Yuan, S. Jia, A. Bansil, F. Chou, H. Lin and M. Z. Hasan, *Nat. Commun.*, 2016, **7**, 10556.
- 19 J. Hu, Z. Tang, J. Liu, X. Liu, Y. Zhu, D. Graf, K. Myhro, S. Tran, C. N. Lau, J. Wei and Z. Mao, *Phys. Rev. Lett.*, 2016, **117**, 016602.
- 20 Y. Hu, S.-S. Li, W.-X. Ji, C.-W. Zhang, M. Ding, P.-J. Wang and S.-S. Yan, *J. Phys. Chem. Lett.*, 2019, **11**, 485.
- 21 Y.-J. Jin, R. Wang, J.-Z. Zhao, Y.-P. Du, C.-D. Zheng, L.-Y. Gan, J.-F. Liu, H. Xu and S. Tong, *Nanoscale*, 2017, **9**, 13112.
- 22 S. Li, Y. Liu, S.-S. Wang, Z.-M. Yu, S. Guan, X.-L. Sheng, Y. Yao and S. A. Yang, *Phys. Rev. B*, 2018, **97**, 045131.
- 23 S.-s. Wang, Z.-m. Yu, Y. Liu, Y. Jiao, S. Guan, X.-l. Sheng and S. A. Yang, *Phys. Rev. Mater.*, 2019, **3**, 084201.
- 24 C. Zhong, W. Wu, J. He, G. Ding, Y. Liu, D. Li, S. A. Yang and G. Zhang, *Nanoscale*, 2019, **11**, 2468.
- 25 N. Zhou, P. Zhou, J. Li, C. He and J. Zhong, *Phys. Rev. B*, 2019, **100**, 115425.
- 26 P. Zhou, Z. Ma and L. Sun, *J. Mater. Chem. C*, 2018, **6**, 1206.
- 27 B. Feng, B. Fu, S. Kasamatsu, S. Ito, P. Cheng, C. C. Liu, Y. Feng, S. Wu, S. K. Mahatha, P. Sheverdyeva, P. Moras, M. Arita, O. Sugino, T. C. Chiang, K. Shimada, K. Miyamoto, T. Okuda, K. Wu, L. Chen, Y. Yao and I. Matsuda, *Nat. Commun.*, 2017, **8**, 1007.
- 28 L. Gao, J. T. Sun, J. C. Lu, H. Li, K. Qian, S. Zhang, Y. Y. Zhang, T. Qian, H. Ding, X. Lin, S. Du and H. J. Gao, *Adv. Mater.*, 2018, **30**, 1707055.
- 29 A. L. Lereu, F. Lemarchand, M. Zerrad, M. Yazdanpanah and A. Passian, *J. Appl. Phys.*, 2015, **117**, 063110.
- 30 Y. Hu, S. S. Li, W. X. Ji, *et al.*, *J. Phys. Chem. Lett.*, 2019, **11**, 485.
- 31 Q. Xia, Y. Hu, Y.-p. Wang, C.-w. Zhang, M.-j. Ren, S.-s. Li and W.-x. Ji, *Nanoscale*, 2022, **14**, 1264.
- 32 G. Kresse and D. Joubert, *Phys. Rev. B: Condens. Matter Mater. Phys.*, 1999, **59**, 1758.
- 33 G. Kresse and J. Furthmüller, *Phys. Rev. B: Condens. Matter Mater. Phys.*, 1996, **54**, 11169.

- 34 G. Kresse and J. Hafner, *Phys. Rev. B: Condens. Matter Mater. Phys.*, 1994, **49**, 14251.
- 35 P. E. Blöchl, *Phys. Rev. B: Condens. Matter Mater. Phys.*, 1994, **50**, 17953.
- 36 S. Grimme, *J. Comput. Chem.*, 2006, **27**, 1787.
- 37 J. P. Perdew and Y. Wang, *Phys. Rev. B: Condens. Matter Mater. Phys.*, 1992, **45**, 13244.
- 38 J. Paier, M. Marsman, K. Hummer, G. Kresse, I. C. Gerber and J. G. Ángyán, *J. Chem. Phys.*, 2006, **124**, 154709.
- 39 T. Tadano, Y. Gohda and S. Tsuneyuki, *J. Phys.: Condens. Matter*, 2014, **26**, 225402.
- 40 Y.-c. Wang, J. Lv, L. Zhu and Y.-m. Ma, *Phys. Rev. B: Condens. Matter Mater. Phys.*, 2010, **82**, 094116.
- 41 Y.-c. Wang, J. Lv, L. Zhu and Y.-m. Ma, *Comput. Phys. Commun.*, 2012, **183**, 2063.
- 42 X.-c. Shao, J. Lv, P. Liu, S. Shao, P.-y. Gao, H.-y. Liu, Y.-c. Wang and Y.-m. Ma, *J. Chem. Phys.*, 2022, **156**, 014105.
- 43 Y.-c. Wang, M.-s. Miao, J. Lv, L. Zhu, K.-t. Yin, H.-y. Liu and Y.-m. Ma, *J. Chem. Phys.*, 2012, **137**, 224108.
- 44 X.-y. Luo, J.-h. Yang, H.-y. Liu, X.-j. Wu, Y.-c. Wang, Y.-m. Ma, S.-h. Wei, X.-g. Gong and H.-j. Xiang, *J. Am. Chem. Soc.*, 2011, **133**, 16285.
- 45 J. Taylor, H. Guo and J. Wang, *Phys. Rev. B: Condens. Matter Mater. Phys.*, 2001, **63**, 245407.
- 46 D. Waldron, P. Haney, B. Larade, A. MacDonald and H. Guo, *Phys. Rev. Lett.*, 2006, **96**, 166804.
- 47 S. Datta, *Electronic transport in mesoscopic systems*, Cambridge University Press, 1997.
- 48 Y. Cheng, X. Wu, Z.-j. Zhang, Y. Sun, Y.-s. Zhao, Y.-y. Zhang and G. Zhang, *Nanoscale*, 2021, **13**, 1425.
- 49 L. Lin, Y. Guo, R. Gillen and R. John, *J. Appl. Phys.*, 2013, **113**, 134103.
- 50 W.-h. Shi, Y.-f. Guo, Z.-h. Zhang and W.-l. Guo, *J. Phys. Chem. Lett.*, 2018, **9**, 6841.
- 51 H. Zhang, C.-X. Liu, X.-L. Qi, X. Dai, Z. Fang and S.-C. Zhang, *Nat. Phys.*, 2009, **5**, 438.
- 52 S. K. Mishra, S. Satpathy and O. Jepsen, *J. Phys.: Condens. Matter*, 1997, **9**, 461.